Title

Surface Morphology and Surface Stability against Oxygen Loss of the Lithium-Excess Li2MnO3 Cathode Material as a Function of Lithium Concentration

Journal

ACS Applied Materials & Interfaces, 8(38)

ISSN

1944-8244

Authors

Shin, Yongwoo
Persson, Kristin A

Publication Date

2016-09-28

DOI

10.1021/acsami.6b07259

Peer reviewed

ACS APPLIED MATERIALS & INTERFACES

Research Article

www.acsami.org

Surface Morphology and Surface Stability against Oxygen Loss of the Lithium-Excess Li_2MnO_3 Cathode Material as a Function of Lithium Concentration

Yongwoo Shin[†] and Kristin A. Persson*[,†,‡]

[†]Energy Storage and Distributed Resources Division, Lawrence Berkeley National Laboratory, Berkeley, California 94720, United States

[‡]Department of Materials Science and Engineering, University of California Berkeley, Berkeley, California 94720, United States

ABSTRACT: There is a growing appreciation for the role of surface reactivity and subsequent reconstruction affecting the performance of high-voltage, high-capacity Li-ion cathode materials. In particular, the promising Li-excess materials are known to exhibit significant vulnerability toward oxygen release, which can cause surface densification and impede Li intercalation. Here we focus on the end member, Li_2MnO_3, as a Li-excess, Mn-rich representative of this class of materials and systematically elucidate all possible stoichiometric low Miller index surfaces with various cation ordering on each surface. We apply surface cation reconstruction rules that depend on the local environment, including target Mn−Li site exchanges, and optimize the resulting surface Li configurations using metadynamics. The equilibrium Wulff shape shows dominant (001), (010) surface facets, and almost all facets exhibit favorable Mn reconstruction. Most importantly, we find that while all equilibrium Li_xMnO_3 surfaces become unstable toward oxygen release for $x <$ 1.7, some facets are consistently more resistant than others which may provide a design metric for more stable particle morphologies and enhanced surface oxygen retention.

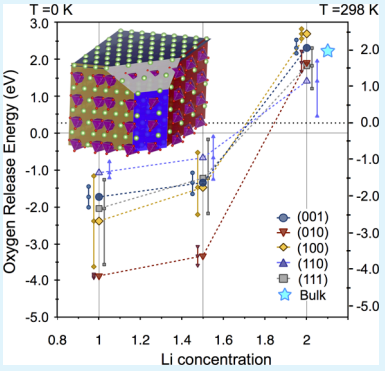

KEYWORDS: *Li-ion battery, cathode, layered Li-excess, surface morphology, oxygen evolution*

1. INTRODUCTION

A materials interaction with the environment can cause chemical as well as structural transformations at the interface, which in turn may influence the long-term performance of the material. Examples are found in a wide range of materials applications such as catalysis, energy storage, and structural materials, etc.[1−5] Specifically, in the energy storage field, the demand for increased energy density is pushing research and development efforts toward high voltage and high capacity which favor materials that are inherently unstable during operating conditions. Indeed, even for commercialized Li-ion cathodes such as $LiNi_xMn_xCo_{1-2x}O_2$ (NMC) there is a growing appreciation for the role of surface reconstruction and passivation in capacity degradation and impedance buildup.[6] Hence, understanding the underlying mechanisms for surface-related decomposition and designing tailored strategies which aim to mitigate the reactivity are important. In particular, the next-generation Li-rich, Mn-rich layered cathode materials[7,8] may benefit from such designs as it is well-known that they are prone to surface oxygen loss.[9−14] For example, Koga et al.[10] found that surface oxygen is oxidized to O_2 and irreversibly lost from Li-excess $Li_{1.20}Mn_{0.54}Co_{0.13}Ni_{0.13}O_2$ during the first cycle. Similarly, Qian et al. reported formation of oxygen vacancies at the surface and within the first five to six subsurface layers in $Li[Li_{1/6}Ni_{1/4}Co_{1/6}Mn_{1/2}]O_2$.[15] Indeed, even bulk reversible oxygen loss[16−18] has, until recently, been one of the suggested mechanisms giving rise to the anomalously high capacity found in Li-excess materials. However, instead it is becoming increasingly accepted that many of the Li-excess materials rely on anion oxidation for charge compensation during the Li extraction.[10,19−24] Adopting either a composite or a solid solution terminology, the end member[25] on the Li-excess spectrum is Li_2MnO_3 (see Figure 1a)[26] which has the highest capacity but also exhibits the worst performance.[27,28] While bulk oxygen redox activity is not necessarily detrimental, in the case of Li_2MnO_3, bulk oxygen oxidation may facilitate Mn migration, subsequent structural deterioration, and voltage fade.[3,4,21,29−32] Furthermore, oxygen loss at the surface can lead to cation migration and densification of the surface and subsurface layers,[10,13,33−35] which is very likely to negatively impact Li transport to/from the particles. Indeed, most studies show that even low-rate, limited cycling of Li_2MnO_3 requires nanoscaling and higher temperatures.[27,30,36] Interestingly, recent experimental as well as theoretical evidence[29,37] indicates that the generally observed poor Li rate performance of Li_2MnO_3 originates from surface passivation and/or particle−particle electrode-level transport limitations. To the best of our knowledge, there are only a few surface reports of Li_2MnO_3. Kim et al.[35] found a majority of (001) and minority (020) (here equivalent to (010)) facets on micrometer-sized Li_2MnO_3

Received: June 15, 2016
Accepted: September 6, 2016

DOI: 10.1021/acsami.6b07259
ACS Appl. Mater. Interfaces XXXX, XXX, XXX−XXX

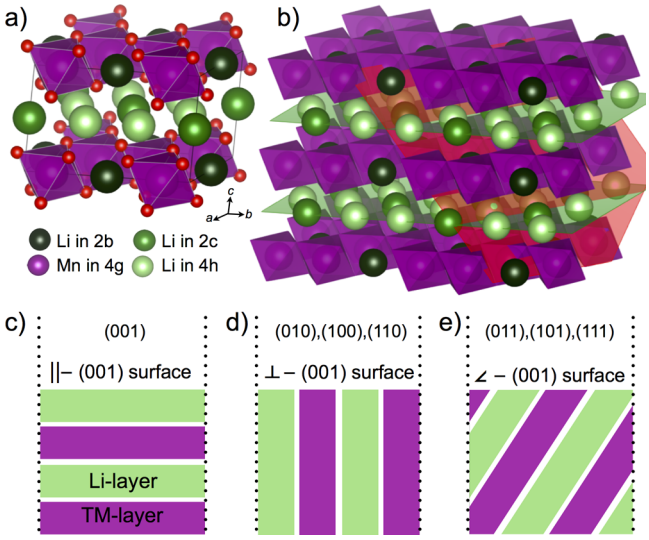

Figure 1. Illustrations of the Li_2MnO_3 bulk as well as surface planes: (a) conventional unit cell structure of Li_2MnO_3; (b) schematics of an arbitrary facet illustrated by the red plane; (c–e) three possible surface groups (||-(001), ⊥-(001), and ∠-(001)) as organized with respect to the relation between their normal and the Li/TM layer stacking direction (001).

particles synthesized at 850 °C. They also investigated Li absorption and mobility on the (001) and (020) Li_2MnO_3 surfaces using computations. Using first-principles density functional theory, we here map out surface stability and vulnerability toward oxygen loss for all low Miller index surface facets of Li_2MnO_3—as a worst-case representative of the family of layered Li-excess materials—to inspire target design of Li-excess cathode materials with improved surface stability and ionic transport. We systematically investigate the most stable crystal facets, as a function of direction, termination, and Li concentration, in order to determine the feasibility of facet stabilization against oxygen release through morphology tuning.

2. RESULTS

In order to calculate the surface energy (γ), we use a slab–vacuum model (see Methods for more details on the calculations) and obtain the surface formation energy as

$$\gamma = \frac{E^{slab} - nE^{bulk}}{2A} \quad (1)$$

Here, E^{slab} is the energy of the slab with a given surface, n is the total number of atoms for the slab, E^{bulk} is the reference bulk energy per atom, and A is the surface area of a given facet. Previous computational surface investigations for other Li-ion cathode materials include the Mn spinel,[38−42] the high-voltage spinel,[43] olivine $LiFePO_4$,[44] and layered $LiCoO_2$.[45−47] In comparison to layered $LiCoO_2$, Li_2MnO_3 includes facets with increased cation mixing due to the excess Li ions in the transition metal (TM) layers. The layered Li-excess family of materials displays various microstructural and compositional features depending on the synthesis procedure[48,49]—however, they share a common layered structure, comprised of a Li layer and a mixed Li/TM layer, where the Li excess is determined by the average amount of Li in the TM layer. In principle, Li_2MnO_3 facets can be terminated through five different atomic combinations such as Li, Mn/Li, O, Li/O, and Li/Mn/O ions. However, the number of stable terminations is governed by the polarity of the surface, as well as the nature and number of under-coordinated surface cations.[50] In the following sections we investigate the most stable terminations for all stoichiometric low Miller index surfaces including (001), (010), (100), (110), (011), (101), and (111). From these results we construct the Wulff shape[51] and subsequently explore the stability of the resulting facets against oxygen release as a function of Li concentration and oxygen chemical potential.

2.1. General Surface Site Preferences and Reconstruction Rules. The low Miller index surfaces of Li_2MnO_3 have seven symmetrically distinguishable facets from the perspective of atomic configuration and crystal symmetry. Figure 1a illustrates the bulk crystal structure, which belongs to the monoclinic $C2/m$ space group, and exhibits two octahedral sites in the Li layer (2c and 4h sites) as well as two octahedral sites in the TM layer (2b and 4g sites). In Li_2MnO_3, one-third of the octahedral sites in the TM layer (2b sites) contain Li ions, which contributes to the mixed cation surface terminations. Any arbitrary facet of Li_2MnO_3, excluding the (001) and (010) surfaces, inevitably includes both Mn and Li ions (see Figure 1b, red plane). All low Miller index surfaces of Li_2MnO_3 can be organized into three distinguishable surface groups (see Figure 1c–e and Table 1) with respect to their relationship between a given surface and the Li layer

Table 1. Calculated Surface Energies of All Low Miller Index Facets Denominated by Their Termination and Tasker Type[a]

surface group	facet	tasker	terminated site (atom)	γ (J/m^2)
||-(001)	001	III	2c–4h (Li)	**0.98**
			2b/4g/4i–8j (Li/Mn/O)	1.92
⊥-(001)	010	II	4h/4g/8j (Li/Mn/O)	**1.27**
			2b–2c/4i (Li/O)	2.32
	100	III	2c–2b–4h/4g (Li/Mn)	**1.30**
			4i–8j (O)	1.83
	110	III	2b–4h/8j (Li/O)	1.98
			2c/4g/4i–8j (Li/Mn/O)	**1.37**
∠-(001)	011	III	2c–2b/8j (Li/O)	1.17
			4h/4g/4i (Li/Mn/O)	1.34
	101	I	2c–4h–2b/4g/4i–8j (Li/Mn/O)	1.50
	111	II	4h/4g/8j (Li/Mn/O)	1.27
			2b–2c/4i (Li/O)	**1.23**

[a]Surface energies shown in bold are exposed in the Wulff structure in Figure 4a.

DOI: 10.1021/acsami.6b07259
ACS Appl. Mater. Interfaces XXXX, XXX, XXX–XXX

percolation direction (or equivalently the TM layer or the $a-b$ plane in Figure 1a). Specifically, the surface normal direction and the direction of the Li layer can be parallel (∥-(001) surfaces (Figure 1c)), perpendicular (⊥-(001) surfaces (Figure 1d)), or slanted angle (∠-(001) surfaces (Figure 1e)) with respect to each other. The ∥-(001) surface group has one surface (001), the ⊥-(001) group has three ((100), (010), and (110)), and finally the ∠-(001) group includes three surfaces ((011), (101), and (111)).

Surface stability depends strongly on the cation arrangement on the surface.[38,39,43,45] Hence, before we examine each individual surface facet cation arrangement, we first perform a systematic investigation to establish general rules for (i) the preferred position of the Li ions on the surface and (ii) the reconstruction of the surface under-coordinated Mn ions. By construction, both ⊥-(001) and the ∠-(001) surface groups exhibit under-coordinated Li as well as Mn surface ions. First, we probe the position preference of Li ions on the (001) surface (see Figure 2a). A Li ion located on top of a 2b site is

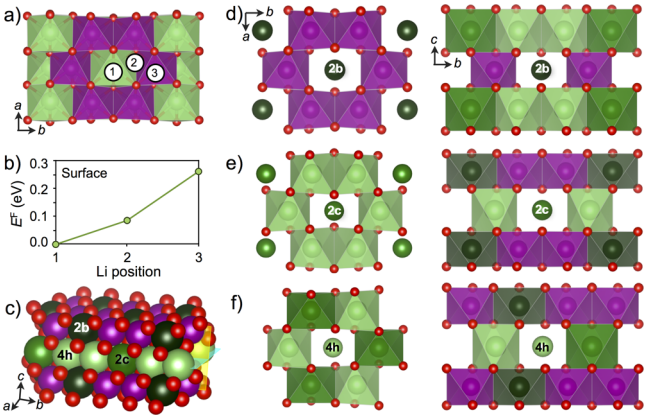

Figure 2. Illustrations of the possible sites for Li ions (green) and Mn ions (purple). The shade or depth of color represents the different Li sites by symmetry. In panel a the possible surface Li sites are shown, with their corresponding energy in panel b. Two representative planes were selected to examine the local environments (c). For surface Mn ions, there are several bulk reconstruction schemes and associated bulk sites possible, as shown in panels d–f, where the left side displays an $a-b$ plane view (cyan plane in panel c) and the right-hand side a $b-c$ plane view (yellow plane in panel c), respectively.

denominated ① and on a 4g site as ③. Position ② indicates a Li ion located on top of the tetrahedral site between the 2b and 4g sites. By examining multiple initial Li-ion arrangements with subsequent ionic relaxation, we find position ① (see Figure 2b) to be the most favorable. This is intuitive since the site ① nearest-neighbor (NN) cation is Li, whereas for the ② and ③ sites the surface Li experiences stronger repulsion from neighboring Mn. These results constitute a general, but not conclusive, rule as different surface facets and terminations include further constraints due to different local cation orderings. In the following steps, we use the rule as a starting point for more detailed investigations of favorable surface Li arrangements. Second, from previous surface investigations[21,38,39,46,47] for $LiMn_2O_4$ spinel and layered $LiCoO_2$ we expect a high energy penalty from under-coordinated, exposed surface TM ions and hence anticipate Mn to either passivate through Li termination (red arrow in Figure 3b) or reconstruct by swapping places with subsurface or bulk Li (black arrow in Figure 3b). The Mn–Li reconstruction scheme was first

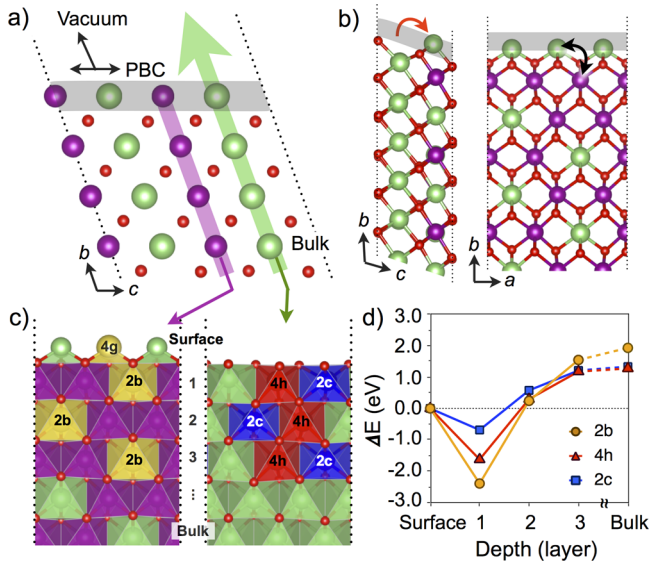

Figure 3. Figures and energetics illustrating the general rules for surface and ion topology. (a) The Li_2MnO_3 ⊥-(001) and the ∠-(001) surface groups exhibit Li percolation paths (green paled arrow) in accordance with the laminating structure. (b) The surface under-coordinated Mn ions are passivated either by exchange with a subsurface Li ion (black arrow) or by moving Li ions (red arrow). (c and d) The surface formation energy is plotted as a function of Mn/Li exchange sites and distance from (100) surface.

suggested by Karim et al.[38] for $LiMn_2O_4$ spinel where it involves exchanging an under-coordinated surface octahedral Mn with a subsurface tetrahedral Li. Recently, this reconstruction was qualitatively validated by the observation of a Mn_3O_4-like surface phase, where Mn occupies both tetrahedral and octahedral sites, in $LiMn_2O_4$ spinel.[52] In the case of layered Li_2MnO_3, both Li and Mn occupy octahedral sites in the same layer, which facilitates a Mn–Li exchange reconstruction. To elucidate the preferred site of Mn defects, as a function of distance from the surface, we investigate the evolution of Mn defect energies from the surface layer to subsurface sites and eventually bulk by replacing a Li ion by a Mn ion (see Figure 3). Three possible sites are the 2b site in the TM layer (yellow octahedron in Figure 3c) or the 4h/2c sites in the Li layer (red/blue octahedron in Figure 3c). Figure 3d shows the (100) surface formation energy as a function of site and depth of the Mn defect from the surface to the bulk. The results clearly show that a Mn–Li exchange can reduce the surface formation energy if a subsurface position is chosen. Swapping a surface Mn with a *bulk* Li is not preferred, as the bulk defect energy penalty overcomes the reduction in surface formation energy. Interestingly, from Figure 3d, we observe that the preferred defect sites ordering between the subsurface and the bulk are different. Panels d–f of Figure 2 illustrate the local environment of the possible Mn bulk defect positions, from two directions. In the bulk, the Mn defect prefers the 4h site which has the least NN Mn ions. As shown in Figure 2d, a 2b Mn defect has six NN Mn, whereas the 2c and 4h sites (see Figure 2e,f, respectively) exhibit four Mn/six Li NN ions and two Mn/eight Li NN ions, respectively. Therefore, the formation energy of the bulk Mn defect (see Figure 2d) closely correlates with the number of neighboring Mn ions (Figure 2d–f). However, this trend is reversed for the surface and subsurface regions. Due to the presence of the surface, which results in under-coordination of certain sites, the cation

DOI: 10.1021/acsami.6b07259
ACS Appl. Mater. Interfaces XXXX, XXX, XXX–XXX

repulsion at the 2b site is decreased which induces a reordering of the stable sites. In summary, we expect surface Li to prefer locations on top of the octahedral sites, neighboring a subsurface Li, and surface Mn to be swapped with subsurface Li 2b sites whenever possible.

2.2. Specific Surface Compositions and Terminations. In accordance with the above established rules, such as surface Li-ion site preference and Mn-ion reconstruction, we now systematically investigate all Li_2MnO_3 low Miller index surfaces and their possible terminations. For each surface facet, we present the resulting surface composition with respect to its termination, reconstruction, and surface cation arrangement. All surfaces and their terminations are classified according to the Tasker classification scheme.[53] Four Li_2MnO_3 surfaces exhibit Tasker type III (see Table 1), which requires the surface dipole to be removed by rearranging 50% of the charge from one surface to the other in the slab−vacuum model maintaining the stoichiometry of the material. The complete surface rearrangement involves (i) moving either Li and/or O ions between the slabs, (ii) swapping any remaining under-coordinated Mn ions with subsurface Li ions, and finally (iii) arranging the remaining surface Li ions using the rule of Figure 2b as an initial guess, but also considering Li−Li interactions specific to the surface facet. However, for some surfaces the complexity of the ionic configurations is particularly challenging. For example, for the (111) surface, in addition to preselecting the sites according to the above rules, we used a simple metadynamics algorithm[54,55] to explore the surface configurational landscape. The metadynamics algorithm was operated via accumulating the artificial penalty functions on the DFT energy landscape until the system evolved from the current local minimum configuration. Table 1 presents a summary of the surface formation energies with respect to their facets, and Figure 4a shows the resulting Wulff shape by a global minimization of the particle total surface energy. Each surface composition is denominated by the available sites of the conventional Li_2MnO_3 unit cell, which are comprised of four Li sites (2c, 2b, and two 4h sites), two Mn sites (4g sites), and six O sites (two 4i and four 8j sites). Figure 4b highlights the resulting exposed ions on each facet of the equilibrium Wulff shape, which provides information about accessible Li-ion channels.

∥-(001) Surface Group. The (001) surface is the only surface in the ∥-(001) surface group and is classified as Tasker type III. The (001) surface lamination layers are composed of positively charged layers with Li ions at 2c−4h sites and negatively charged layers with Li/Mn/O ions at 2b/4g/4i−8j sites. Possible terminations include only Li ions or combined Li/Mn/O ions. Both terminations require removal of the Tasker III dipole which is achieved by a rearrangement of charge between the two slab surfaces. The most stable surface Li configuration on the positively charged surface termination was found to be one-third Li ions located on ① sites and two-thirds Li ions located on ② sites (see Figure 2a) . For the negatively charged Li/Mn/O surface termination we employ Mn reconstruction, as the available surface Li/O ions proved insufficient to passivate the surface Mn ions. As a result, and as noted in Table 1, the most stable termination for the (001) surface is given by the Li termination by almost 1 J/m^2.

⊥-(001) Surface Group. The ⊥-(001) surface group contains the (010), (100), and (110) surfaces which exhibit Li percolation channels perpendicular to the surfaces (see pale green arrow in Figure 3a). While the (010) surface belongs to the Tasker II type, the (100) and the (110) surfaces are both

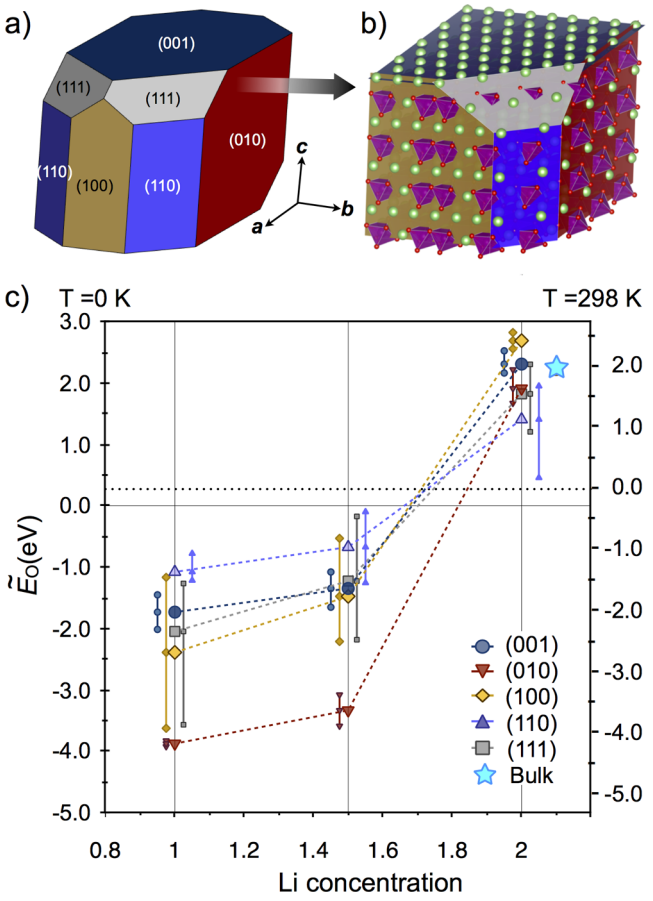

Figure 4. (a) Wulff shape of Li_2MnO_3 and (b) exposed atomic species of each surface; (c) average single surface vacancy oxygen release energy ($\tilde{E}_O$) for each surface facet as indicated by the different symbols. The error bar represents the spread of values as given by the maximum and minimum oxygen release energies for the given surface, respectively.

classified as Tasker type III and hence require rearrangement of the charge (here Li ions) between the two slabs.

The (010) surface exhibits two different laminations with a periodicity of three and is classified as Tasker type II. The positively charged layer contains Li/Mn/O ions at $\frac{1}{2}$4h/$\frac{1}{2}$4g/$\frac{1}{2}$8j sites, and the negatively charged layer contains Li/O ions at 2b−2c/4i sites. By optimizing the Li-ion positions and reconstructing under-coordinated Mn ions, we find the Li/Mn/O-terminated (010) surface to be the most stable, and indeed one of the most stable surfaces of Li_2MnO_3 (see Figure 4a).

The (100) surface has two lamination layers perpendicular to the surface normal (see Figure 1d), with Li/Mn cations on the 2c−2b−4h/4g sites and O anions on the 4i−8j sites. For both the anion- and the cation-terminated surface, either O and/or Mn/Li ions need to be displaced to remove the dipole. Displacing the O ions leads to an increased number of under-coordinated Mn which all need to be reconstructed using the Mn−Li swapping scheme. Systematically examining the resulting dipole-corrected slabs with subsequent Mn reconstructions as well as Li decorations indicates that the Li/Mn cation-terminated surface with Mn reconstruction is the energetically more favorable.

DOI: 10.1021/acsami.6b07259
ACS Appl. Mater. Interfaces XXXX, XXX, XXX−XXX

The (110) surface exhibits two lamination layers, where the positively and negatively charged layers contain both cations and anions in a single layer, resulting in Li/O- and Li/Mn/O-terminated surfaces (see Table 1). Similar to the other facets, the surface Li positions are optimized and under-coordinated Mn swapped with subsurface Li ions. The resulting most stable termination is found to be Li/Mn/O with reconstructed Mn ions.

∠ -(001) Surface Group. The (011), (101), and (111) surfaces all belong to the∠-(001) surface group where the Li percolation direction exhibits a slanted angle with respect to the surface normal. According to the Tasker criteria the (011) surface is type III, the (101) surface is type I, and the (111) surface is type II.

The (011) surface exhibits two lamination layers which are composed of negatively charged 2c/2b/8j sites and positively charged 4h/4g/4i sites. The Li/O termination with a 2c−2b/8j sites layer exhibits a relatively low energy, in fact second lowest among all the considered facets; however, because of its direction, the (011) surface is not favorable in the Wulff construction.

The (101) surface is the only Tasker I surface among the low Miller index surfaces and exhibits only one possible termination: Li/Mn/O. Despite Mn reconstruction and surface Li arrangement optimization, the (101) surface is found to be the most unstable among the examined surface facets.

The (111) surface exhibits a periodicity of three alternatively charged layers, corresponding to positively charged first and third layers with Li/Mn/O at $\frac{1}{2}$4h/$\frac{1}{2}$4g/$\frac{1}{2}$8j sites, and a negatively charged second layer with Li/O at 2b−2c/4i sites. The (111) surface exhibits the only termination where Mn is not favoring reconstruction using the Mn−Li exchange. Instead, the most stable surface cation arrangement consists of tetravalent square pyramidal Mn sites under stoichiometric conditions.

2.3. Oxygen Evolutions on the Low Miller Index Surfaces. From the results in section 2.2 we obtain a ranking of the low Miller index Li_2MnO_3 surfaces (Table 1) and hence an estimated equilibrium particle shape under stoichiometric conditions. To examine the particle vulnerability toward surface oxygen loss, we systematically remove oxygen ions—one at a time—from the different facets appearing in the Wulff shape and record the energy of removal as a function of Li content. The Li cation arrangement in the bulk, as a function of Li content, is kept compliant with previous bulk Li_xMnO_3 investigations.[21,37] Specifically, some Li in the 4h sites are extracted in the early delithiation process ($1.75 < x < 2.0$), some Li in the 4h and 2b sites are extracted for $1.5 < x < 1.75$, and afterward, some 2b Li and all 2c Li are extracted for $1.25 < x < 1.5$. Finally, all Li in the 2b sites are extracted in the range $1.0 < x < 1.25$. At $x = 1$, the remaining Li are all occupying 4h sites in the Li layer. As previously mentioned, when Li is removed from this material, the charge compensation mechanism[10,19−22] is centered on the anion. Hence, O^{1-} species will form on the surface for lower Li contents and those—together with under-coordinated oxygens—are prioritized for removal. However, all possible surface single oxygen vacancies are examined. The oxygen evolution on each surface facet is calculated as the oxygen release energy;

$$\tilde{E}_O = E^{slab}_{O-x'} + \Delta\mu_O - E^{slab} \quad (2)$$

where $E^{slab}_{O-x'}$ defined as the x' oxygen deficient slab energy, and the oxygen chemical potential is defined as $\Delta\mu_O = \mu_O - \mu^*$. Here, the overestimated O_2 binding energy was corrected in accordance with previous work, introducing the reference chemical potential (μ^*), which is obtained by calibrating the formation enthalpies with experimental measurements of various oxides.[56,57] The temperature effect on gas phase oxygen is applied through the oxygen chemical potential, such that two representative temperatures (0 K and room temperature) are indicated on the left- and right-hand side of the y-axis in Figure 4c. The oxygen release, as a function of Li concentration, is recorded as an average over all the single oxygen vacancies on the surface, and the spread in values between different sites is indicated as an error bar on the average. The results, for each considered surface facet, are presented in Figure 4c for various Li concentrations. To provide a comparative value, the oxygen vacancy formation energy in the bulk is provided by the star mark and is calculated as the mean value of a single oxygen vacancy at the 4i and 8j sites, respectively.

In the fully lithiated system (i.e., a Li concentration corresponding to $x = 2.0$), the oxygen release energies of all surfaces exhibit positive values, which indicates that the as-made material is stable against spontaneous surface oxygen evolution, and quite similar (within the accuracy of the calculations) to the bulk oxygen vacancy formation energy. However, as Li is extracted from the material, surface oxygen release very rapidly becomes thermodynamically favorable. Previous work[21] showed that bulk Li_2MnO_3 becomes unstable toward oxygen release for $x < 1$. Indeed, our previous calculations of bulk Li_xMnO_3[21] resulted in oxygen release energies corresponding to 0.4 eV ($x = 1.0$) and 2.6 eV ($x = 2.0$) per oxygen at 0 K, which is comparable to current work for the bulk at $x = 2.0$ (cyan star in Figure 4c). The small difference is attributed to the slight change in the U parameter as compared to previous work ($U = 3.9$ eV here as compared to previously used $U = 4.5$ eV). In comparison with bulk oxygen evolution,[21] where the oxygen is more tightly bound to the lattice, here we find that all stable surfaces are unstable toward oxygen release for $x < 1.7$, e.g., much closer to the fully lithiated material. Indeed, it has been experimentally observed[3] that oxygen evolution initiates at 19% of Li extraction (i.e., $Li_{1.63}MnO_3$), which agrees very well with our examination. The results of Figure 4c suggest that there is no equilibrium low Miller Index Li_2MnO_3 facet that is stable against oxygen release as Li is withdrawn from the structure. However, some facets are more stable than others, which may provide a design metric for morphology tuning toward enhanced, albeit not complete, surface oxygen retention. For example, we note that the (110) surface is consistently more stable than the other facets, and conversely, the (010) facet is the most unstable. Hence we would expect Li_2MnO_3 particles with minimized (010) surfaces and enhanced (110) facets to exhibit improved oxygen retention.

3. DISCUSSION AND CONCLUSION

Using first-principles density functional theory, we mapped out the surface facet stability and vulnerability toward oxygen loss of Li_2MnO_3—as a worst-case representative of the family of layered Li-excess materials—to inspire target design of Li-excess cathode materials with improved surface stability and ionic transport. All facets are rigorously investigated for different cation orderings including Mn reconstruction involving the exchange of subsurface Li and optimal Li surface

DOI: 10.1021/acsami.6b07259
ACS Appl. Mater. Interfaces XXXX, XXX, XXX−XXX

configuration. All surfaces except the (111) exhibit favorable reconstructed Mn; however, only subsurface exchange is favorable—exchange between surface Mn and bulk Li is found to be energetically unfavorable, which indicates that the reconstruction is limited to the surface region. Dominating facets are (001)—similar to $LiCoO_2$[45]—and (110) as well as (100) facets which provide excellent access to Li percolation paths. Previous experimental investigations by Kim et al.[35] found a majority of (001) and minority (020) (equivalent to (010)) facets on micrometer-sized Li_2MnO_3 particles synthesized at 850 °C, which is in excellent agreement with the resulting particle shape.

Furthermore, as many Li-ion cathode materials are known to exhibit surface oxygen loss during the first cycles of operation,[9−14] we extend our investigation to surface stability against oxygen release. In the case of Li-excess materials, this degradation process is pronounced as one of the charge compensation mechanisms in this class of materials provided by the anion, e.g., oxygen oxidation.[10,19−24] Hence, surface oxygen release is accelerated through the formation of O^{1-} species which are less strongly bound to the underlying lattice compared to O^{2-}. Indeed, previous work on Li-excess cathodes, such as $Li_{1.20}Mn_{0.54}Co_{0.13}Ni_{0.13}O_2$ and Li-$[Li_{1/6}Ni_{1/4}Co_{1/6}Mn_{1/2}]O_2$, showed significant loss of surface oxygen during the first cycles, while none in the bulk region of the material.[10,15] We calculated the oxygen release energy as a function of Li content, averaged over all possible single surface oxygen vacancies. We found that while Li_xMnO_3 exhibits stable surface oxygen for $x = 2$ under normal oxygen chemical potential conditions, any Li removal beyond $x = 1.7$ renders all considered low-energy facets thermodynamically unstable toward oxygen release. This is corroborated by Wang et al.[3] who recorded oxygen evolution starting at 19% Li extraction (i.e., $Li_{1.63}MnO_3$). In particular, we find that the (010), (100), and (111) surfaces are more prone to oxygen loss as compared to the (001) and the (110) surfaces. This is in agreement with experimental observations such that the surface degradation of the (001) surface is slower than other surfaces.[4] Significant loss of surface oxygen is likely to cause surface reconstruction, transition metal migration, and densification which can create a bottleneck for ionic conductivity and cause impedance rise. Hence, based on the evidence we find it plausible that pronounced surface oxygen loss constitutes one of the main culprits for the poor initial performance of Li-excess materials, in particular Li_2MnO_3. Indeed, a recent investigation by the authors[37] indicated that the bulk ionic mobility in Li_2MnO_3 is on par with $LiCoO_2$ Li diffusivity, which suggests that the reason for its observed poor rate performance originates either from the surface and/or interparticle transport limitations. This is indirectly supported by recent work by Croy et al.[58] showing that carbon pretreatment of micrometer-sized Li_2MnO_3 significantly improves its performance. We speculate that while the carbon pretreatment cannot impact the electronic or ionic conductivity of bulk micrometer-sized particles, it may decrease the reactivity of the surface and/or enhance particle−particle transport.

In conclusion, we found that all equilibrium surface facets of Li_2MnO_3 become vulnerable toward oxygen loss even for modest removal of Li. Hence, while morphology tuning may provide a mitigating strategy, it is unlikely to provide a mechanism to fully retain surface oxygen in high-Li-excess materials. Recommended strategies therefore include coatings that are impenetrable for oxygen diffusion or solid-state electrolyte approaches.

4. METHODS

Our slab model contained more than 10 bulk layers with fixed atomic coordinates taken from previous bulk examinations. The first five surface and subsurface layers are fully relaxed, and the slab is terminated by more than a 15 Å vacuum interval. The total energy results were calculated using density functional theory (DFT) as implemented by the Vienna ab inito simulation package (VASP)[59−62] with the projector augmented wave (PAW)[63,64] pseudopotential method. The exchange correlation functional is chosen as the generalized gradient approximation (GGA+U)[65−67] with an on-site Hubbard parameter (U_{Mn} = 3.9 eV[68]). The calculations were converged within 1 meV, enabled by a cutoff energy of 520 eV with an adjusted k-point sampling density with respect to the size of supercells. The cell parameters of stoichiometric Li_2MnO_3 were downloaded from the Materials Project ($ID_{Li_2MnO_3}$: mp-18988).[68,69]

AUTHOR INFORMATION

Corresponding Author

*E-mail: kapersson@lbl.gov. Phone: +1 (510) 486-7218.

Notes

The authors declare no competing financial interest.

ACKNOWLEDGMENTS

Y.S. gratefully acknowledges Dr. Muratahan Aykol for his helpful comments and discussions. This work was intellectually led by the Battery Materials Research (BMR) program, under the Assistant Secretary for Energy Efficiency and Renewable Energy, Office of Vehicle Technologies of the U.S. Department of Energy, Contract No. DE-AC02-05CH11231. Finally, this research used resources of the National Energy Research Scientific Computing Center (NERSC).

REFERENCES

(1) Bell, A. T. The Impact of Nanoscience on Heterogeneous Catalysis. *Science* **2003**, *299*, 1688−1691.

(2) Karim, W.; Kleibert, A.; Hartfelder, U.; Balan, A.; Gobrecht, J.; van Bokhoven, J. A.; Ekinci, Y. Size-Dependent Redox Behavior of Iron Observed by in-Situ Single Nanoparticle Spectro-microscopy on Well-Defined Model Systems. *Sci. Rep.* **2016**, *6*, 18818.

(3) Wang, R.; He, X.; He, L.; Wang, F.; Xiao, R.; Gu, L.; Li, H.; Chen, L. Atomic Structure of Li_2MnO_3 after Partial Delithiation and Re-Lithiation. *Adv. Energy Mater.* **2013**, *3*, 1358−1367.

(4) Yan, P.; Xiao, L.; Zheng, J.; Zhou, Y.; He, Y.; Zu, X.; Mao, S. X.; Xiao, J.; Gao, F.; Zhang, J.-G.; Wang, C.-M. Probing the Degradation Mechanism of Li_2MnO_3 Cathode for Li-Ion Batteries. *Chem. Mater.* **2015**, *27*, 975−982.

(5) Zheng, J.; Gu, M.; Xiao, J.; Zuo, P.; Wang, C.; Zhang, J.-G. Corrosion/Fragmentation of Layered Composite Cathode and Related Capacity/Voltage Fading during Cycling Process. *Nano Lett.* **2013**, *13*, 3824−3830.

(6) Lin, F.; Markus, I. M.; Nordlund, D.; Weng, T.-C.; Asta, M. D.; Xin, H. L.; Doeff, M. M. Surface Reconstruction and Chemical Evolution of Stoichiometric Layered Cathode Materials for Lithium-Ion Batteries. *Nat. Commun.* **2014**, *5*, 3529.

(7) Thackeray, M. M.; Kang, S.-H.; Johnson, C. S.; Vaughey, J. T.; Benedek, R.; Hackney, S. A. Li_2MnO_3-stabilized $LiMO_2$ (M = Mn, Ni, Co) Electrodes for Lithium-ion Batteries. *J. Mater. Chem.* **2007**, *17*, 3112−15.

(8) Hong, J.; Gwon, H.; Jung, S.-K.; Ku, K.; Kang, K. Review—Lithium-Excess Layered Cathodes for Lithium Rechargeable Batteries. *J. Electrochem. Soc.* **2015**, *162*, A2447−A2467.

(9) Armstrong, A. R.; Holzapfel, M.; Novák, P.; Johnson, C. S.; Kang, S.-H.; Thackeray, M. M.; Bruce, P. G. Demonstrating Oxygen Loss

DOI: 10.1021/acsami.6b07259
ACS Appl. Mater. Interfaces XXXX, XXX, XXX−XXX

and Associated Structural Reorganization in the Lithium Battery Cathode $Li[Ni_{0.2}Li_{0.2}Mn_{0.6}]O_2$. *J. Am. Chem. Soc.* **2006**, *128*, 8694−8698.
(10) Koga, H.; Croguennec, L.; Ménétrier, M.; Mannessiez, P.; Weill, F.; Delmas, C. Different Oxygen Redox Participation for Bulk and Surface: A Possible Global Explanation for the Cycling Mechanism of $Li_{1.20}Mn_{0.54}Co_{0.13}Ni_{0.13}O_2$. *J. Power Sources* **2013**, *236*, 250−258.
(11) Boulineau, A.; Croguennec, L.; Delmas, C.; Weill, F. Structure of Li_2MnO_3 with Different Degrees of Defects. *Solid State Ionics* **2010**, *180*, 1652−1659.
(12) Boulineau, A.; Croguennec, L.; Delmas, C.; Weill, F. Reinvestigation of Li_2MnO_3 Structure: Electron Diffraction and High Resolution TEM. *Chem. Mater.* **2009**, *21*, 4216−4222.
(13) Xu, B.; Fell, C. R.; Chi, M.; Meng, Y. S. Identifying Surface Structural Changes in Layered Li-excess Nickel Manganese Oxides in High Voltage Lithium Ion Batteries: A Joint Experimental and Theoretical Study. *Energy Environ. Sci.* **2011**, *4*, 2223−2233.
(14) Jiang, M.; Key, B.; Meng, Y. S.; Grey, C. P. Electrochemical and Structural Study of the Layered, "Li-Excess" Lithium-Ion Battery Electrode Material $Li[Li_{1/9}Ni_{1/3}Mn_{5/9}]O_2$. *Chem. Mater.* **2009**, *21*, 2733−2745.
(15) Qian, D.; Xu, B.; Chi, M.; Meng, Y. S. Uncovering the Roles of Oxygen Vacancies in Cation Migration in Lithium Excess Layered Oxides. *Phys. Chem. Chem. Phys.* **2014**, *16*, 14665−14668.
(16) van Bommel, A.; Dahn, J. R. Kinetics Study of the High Potential Range of Lithium-Rich Transition-Metal Oxides for Lithium-Ion Batteries by Electrochemical Methods. *Electrochem. Solid-State Lett.* **2010**, *13*, A62−3.
(17) Lu, Z.; Dahn, J. R. Understanding the Anomalous Capacity of $Li/Li[Ni_xLi_{(1/3-2x/3)}Mn_{(2/3-x/3)}]O_2$ Cells Using In Situ X-Ray Diffraction and Electrochemical Studies. *J. Electrochem. Soc.* **2002**, *149*, A815−8.
(18) Muhammad, S.; Kim, H.; Kim, Y.; Kim, D.; Song, J. H.; Yoon, J.; Park, J.-H.; Ahn, S.-J.; Kang, S.-H.; Thackeray, M. M.; Yoon, W.-S. Evidence of Reversible Oxygen Participation in Anomalously High Capacity Li- and Mn-rich Cathodes for Li-ion Batteries. *Nano Energy* **2016**, *21*, 172−184.
(19) Armand, M.; Tarascon, J.-M. Building Better Batteries. *Nature* **2008**, *451*, 652−657.
(20) Bréger, J.; Meng, Y. S.; Hinuma, Y.; Kumar, S.; Kang, K.; Shao-Horn, Y.; Ceder, G.; Grey, C. P. Effect of High Voltage on the Structure and Electrochemistry of $LiNi_{0.5}Mn_{0.5}O_2$: A Joint Experimental and Theoretical Study. *Chem. Mater.* **2006**, *18*, 4768−4781.
(21) Lee, E.; Persson, K. A. Structural and Chemical Evolution of the Layered Li-Excess Li_xMnO_3 as a Function of Li Content from First-Principles Calculations. *Adv. Energy Mater.* **2014**, *4*, 1400498.
(22) Richards, W. D.; Tsujimura, T.; Miara, L. J.; Wang, Y.; Kim, J. C.; Ong, S. P.; Uechi, I.; Suzuki, N.; Ceder, G. Design and Synthesis of the Superionic Conductor $Na_{10}SnP_2S_{12}$. *Nat. Commun.* **2016**, *7*, 11009.
(23) Seo, D.-H.; Lee, J.; Urban, A.; Malik, R.; Kang, S.; Ceder, G. The Structural and Chemical Origin of the Oxygen Redox Activity in Layered and Cation-Disordered Li-Excess Cathode Materials. *Nat. Chem.* **2016**, *8*, 692−697.
(24) Luo, K.; Roberts, M. R.; Hao, R.; Guerrini, N.; Pickup, D. M.; Liu, Y.-S.; Edström, K.; Guo, J.; Chadwick, A. V.; Duda, L. C.; Bruce, P. G. Charge-compensation in 3*d*-Transition-Metal-Oxide Intercalation Cathodes through the Generation of Localized Electron Holes on Oxygen. *Nat. Chem.* **2016**, *8*, 684−691.
(25) Ellis, B. L.; Lee, K. T.; Nazar, L. F. Positive Electrode Materials for Li-Ion and Li-Batteries. *Chem. Mater.* **2010**, *22*, 691−714.
(26) Rossouw, M. H.; Thackeray, M. M. Lithium Manganese Oxides from Li_2MnO_3 for Rechargeable Lithium Battery Applications. *Mater. Res. Bull.* **1991**, *26*, 463−473.
(27) Marom, R.; Amalraj, S. F.; Leifer, N.; Jacob, D.; Aurbach, D. A Review of Advanced and Practical Lithium Battery Materials. *J. Mater. Chem.* **2011**, *21*, 9938−17.
(28) Johnson, C. S.; Li, N.; Vaughey, J. T.; Hackney, S. A.; Thackeray, M. M. Lithium−manganese Oxide Electrodes with Layered−spinel Composite Structures $xLi_2MnO_3\cdot(1-x)Li_{1+y}Mn_{2-y}O_4$ ($0 < x < 1$, $0 \le y \le 0.33$) for Lithium Batteries. *Electrochem. Commun.* **2005**, *7*, 528−536.
(29) Croy, J. R.; Iddir, H.; Gallagher, K.; Johnson, C. S.; Benedek, R.; Balasubramanian, M. First-charge Instabilities of Layered-layered Lithium-ion-battery Materials. *Phys. Chem. Chem. Phys.* **2015**, *17*, 24382−24391.
(30) Li, Y.; Bareno, J.; Bettge, M.; Abraham, D. P. Unexpected Voltage Fade in LMR-NMC Oxides Cycled below the "Activation" Plateau. *J. Electrochem. Soc.* **2015**, *162*, A155−A161.
(31) Kan, Y.; Hu, Y.; Lin, C.-K.; Ren, Y.; Sun, Y.-K.; Amine, K.; Chen, Z. Migration of Mn Cations in Delithiated Lithium Manganese Oxides. *Phys. Chem. Chem. Phys.* **2014**, *16*, 20697−20702.
(32) Amalraj, S. F.; Markovsky, B.; Sharon, D.; Talianker, M.; Zinigrad, E.; Persky, R.; Haik, O.; Grinblat, J.; Lampert, J.; Schulz-Dobrick, M.; Garsuch, A.; Burlaka, L.; Aurbach, D. Study of the Electrochemical Behavior of the "Inactive" Li_2MnO_3. *Electrochim. Acta* **2012**, *78*, 32−39.
(33) Fell, C. R.; Chi, M.; Meng, Y. S.; Jones, J. L. In Situ X-ray Diffraction Study of the Lithium Excess Layered Oxide Compound $Li[Li_{0.2}Ni_{0.2}Mn_{0.6}]O_2$ During Electrochemical Cycling. *Solid State Ionics* **2012**, *207*, 44−49.
(34) Fell, C. R.; Qian, D.; Carroll, K. J.; Chi, M.; Jones, J. L.; Meng, Y. S. Correlation Between Oxygen Vacancy, Microstrain, and Cation Distribution in Lithium-Excess Layered Oxides During the First Electrochemical Cycle. *Chem. Mater.* **2013**, *25*, 1621−1629.
(35) Kim, D.; Lim, J.-M.; Lim, Y.-G.; Park, M.-S.; Kim, Y.-J.; Cho, M.; Cho, K. Understanding of Surface Redox Behaviors of Li_2MnO_3 in Li-Ion Batteries: First-Principles Prediction and Experimental Validation. *ChemSusChem* **2015**, *8*, 3255−3262.
(36) Dong, X.; Xu, Y.; Yan, S.; Mao, S.; Xiong, L.; Sun, X. Towards Low-cost, High Energy Density Li_2MnO_3 Cathode Materials. *J. Mater. Chem. A* **2015**, *3*, 670−679.
(37) Shin, Y.; Ding, H.; Persson, K. A. Revealing the Intrinsic Li Mobility in the Li_2MnO_3 Lithium-Excess Material. *Chem. Mater.* **2016**, *28*, 2081−2088.
(38) Karim, A.; Fosse, S.; Persson, K. A. Surface Structure and Equilibrium Particle Shape of the $LiMn_2O_4$ Spinel from First-Principles Calculations. *Phys. Rev. B: Condens. Matter Mater. Phys.* **2013**, *87*, 075322.
(39) Warburton, R. E.; Iddir, H.; Curtiss, L. A.; Greeley, J. Thermodynamic Stability of Low- and High-Index Spinel $LiMn_2O_4$ Surface Terminations. *ACS Appl. Mater. Interfaces* **2016**, *8*, 11108−11121.
(40) Kim, S.; Aykol, M.; Wolverton, C. Surface Phase Diagram and Stability of (001) and (111) $LiMn_2O_4$ Spinel Oxides. *Phys. Rev. B: Condens. Matter Mater. Phys.* **2015**, *92*, 115411.
(41) Benedek, R.; Thackeray, M. M. Simulation of the Surface Structure of Lithium Manganese Oxide Spinel. *Phys. Rev. B: Condens. Matter Mater. Phys.* **2011**, *83*, 195439.
(42) Ouyang, C. Y.; Zeng, X. M.; Šljivancanin, Ž; Baldereschi, A. Oxidation States of Mn Atoms at Clean and Al_2O_3-Covered $LiMn_2O_4$ (001) Surfaces. *J. Phys. Chem. C* **2010**, *114*, 4756−4759.
(43) Lee, E.; Persson, K. A. First-principles Study of the Nano-scaling Effect on the Electrochemical Behavior in $LiNi_{0.5}Mn_{1.5}O_4$. *Nanotechnology* **2013**, *24*, 424007.
(44) Wang, L.; Zhou, F.; Meng, Y. S.; Ceder, G. First-Principles Study of Surface Properties of $LiFePO_4$: Surface Energy, Structure, Wulff Shape, and Surface Redox Potential. *Phys. Rev. B: Condens. Matter Mater. Phys.* **2007**, *76*, 165435.
(45) Kramer, D.; Ceder, G. Tailoring the Morphology of $LiCoO_2$: A First Principles Study. *Chem. Mater.* **2009**, *21*, 3799−3809.
(46) Dahéron, L.; Martinez, H.; Dedryvère, R.; Baraille, I.; Menetrier, M.; Denage, C.; Delmas, C.; Gonbeau, D. Surface Properties of $LiCoO_2$ Investigated by XPS Analyses and Theoretical Calculations. *J. Phys. Chem. C* **2009**, *113*, 5843−5852.
(47) Kim, Y.; Lee, H.; Kang, S. First-principles and Experimental Investigation of the Morphology of Layer-structured $LiNiO_2$ and $LiCoO_2$. *J. Mater. Chem.* **2012**, *22*, 12874−8.

DOI: 10.1021/acsami.6b07259
ACS Appl. Mater. Interfaces XXXX, XXX, XXX−XXX

(48) Thackeray, M. M.; Johnson, C. S.; Vaughey, J. T.; Li, N.; Hackney, S. A. Advances in Manganese-Oxide 'Composite' Electrodes for Lithium-Ion Batteries. *J. Mater. Chem.* **2005**, *15*, 2257−2267.
(49) Johnson, C. S.; Kim, J.-S.; Lefief, C.; Li, N.; Vaughey, J. T.; Thackeray, M. M. The Significance of the Li_2MnO_3 Component in 'composite' $xLi_2MnO_3 \cdot (1-x)LiMn_{0.5}Ni_{0.5}O_2$ Electrodes. *Electrochem. Commun.* **2004**, *6*, 1085−1091.
(50) Kung, H. H. *Transition Metal Oxides: Surface Chemistry and Catalysis*; Elsevier: Amsterdam, 1989; Vol. *45*.
(51) Wulff, G. On the Question of Speed of Growth and Dissolution of Crystal Surfaces. *Z. Kristallogr.* **1901**, *34*, 449−530.
(52) Amos, C. D.; Roldan, M. A.; Varela, M.; Goodenough, J. B.; Ferreira, P. J. Revealing the Reconstructed Surface of $Li[Mn_2]O_4$. *Nano Lett.* **2016**, *16*, 2899−2906.
(53) Tasker, P. W. The Stability of Ionic Crystal Surfaces. *J. Phys. C: Solid State Phys.* **1979**, *12*, 4977−4984.
(54) Laio, A.; Parrinello, M. Escaping Free-energy Minima. *Proc. Natl. Acad. Sci. U. S. A.* **2002**, *99*, 12562−12566.
(55) Kushima, A.; Lin, X.; Li, J.; Eapen, J.; Mauro, J. C.; Qian, X.; Diep, P.; Yip, S. Computing the Viscosity of Supercooled Liquids. *J. Chem. Phys.* **2009**, *130*, 224504−12.
(56) Wang, L.; Maxisch, T.; Ceder, G. Oxidation Energies of Transition Metal Oxides within the GGA + U Framework. *Phys. Rev. B: Condens. Matter Mater. Phys.* **2006**, *73*, 195107.
(57) Aykol, M.; Wolverton, C. Local Environment Dependent GGA + U Method for Accurate Thermochemistry of Transition Metal Compounds. *Phys. Rev. B: Condens. Matter Mater. Phys.* **2014**, *90*, 115105.
(58) Croy, J. R.; Park, J. S.; Dogan, F.; Johnson, C. S.; Key, B.; Balasubramanian, M. First-Cycle Evolution of Local Structure in Electrochemically Activated Li_2MnO_3. *Chem. Mater.* **2014**, *26*, 7091−7098.
(59) Kresse, G.; Hafner, J. *Ab initio* Molecular Dynamics for Liquid Metals. *Phys. Rev. B: Condens. Matter Mater. Phys.* **1993**, *47*, 558−561.
(60) Kresse, G.; Hafner, J. *Ab initio* Molecular-dynamics Simulation of the Liquid-metal-amorphous-semiconductor Transition in Germanium. *Phys. Rev. B: Condens. Matter Mater. Phys.* **1994**, *49*, 14251−14269.
(61) Kresse, G.; Furthmuller, J. Efficiency of ab-Initio Total Energy Calculations for Metals and Semiconductors using a Plane-Wave Basis Set. *Comput. Mater. Sci.* **1996**, *6*, 15−50.
(62) Kresse, G.; Furthmüller, J. Efficient Iterative Schemes for *ab initio* Total-energy Calculations using a Plane-wave Basis Set. *Phys. Rev. B: Condens. Matter Mater. Phys.* **1996**, *54*, 11169−11186.
(63) Blöchl, P. E. Projector Augmented-wave Method. *Phys. Rev. B: Condens. Matter Mater. Phys.* **1994**, *50*, 17953−17979.
(64) Kresse, G.; Joubert, D. From Ultrasoft Pseudopotentials to the Projector Augmented-wave Method. *Phys. Rev. B: Condens. Matter Mater. Phys.* **1999**, *59*, 1758−1775.
(65) Perdew, J. P.; Burke, K.; Ernzerhof, M. Generalized Gradient Approximation Made Simple. *Phys. Rev. Lett.* **1996**, *77*, 3865−3868.
(66) Perdew, J. P.; Burke, K.; Ernzerhof, M. Generalized Gradient Approximation Made Simple [Phys. Rev. Lett. 77, 3865 (1996)]. *Phys. Rev. Lett.* **1997**, *78*, 1396−1396.
(67) Liechtenstein, A. I.; Anisimov, V. I.; Zaanen, J. Density-Functional Theory and Strong Interactions: Orbital Ordering in Mott-Hubbard Insulators. *Phys. Rev. B: Condens. Matter Mater. Phys.* **1995**, *52*, R5467−R5470.
(68) Jain, A.; Ong, S. P.; Hautier, G.; Chen, W.; Richards, W. D.; Dacek, S.; Cholia, S.; Gunter, D.; Skinner, D.; Ceder, G.; Persson, K. a The Materials Project: A Materials Genome Approach to Accelerating Materials Innovation. *APL Mater.* **2013**, *1*, 011002.
(69) *Materials Project*, ID for Li_2MnO_3,: mp-18988; Lawrence Berkeley National Laboratory: Berkeley, CA, USA, 2014; DOI: 10.17188/1193768.

DOI: 10.1021/acsami.6b07259
ACS Appl. Mater. Interfaces XXXX, XXX, XXX−XXX